Astron. Astrophys. 363, 575–584 (2000)

ASTRONOMY AND ASTROPHYSICS

The optical, X-ray and gamma-ray light curves and spectra of crab-like pulsars: PSR B0540-69 and PSR B1509-58

L. Zhang[1,2] **and K.S. Cheng**[1]

[1] The University of Hong Kong, Department of Physics, P.R. China
[2] Yunnan University, Department of Physics, Kunming, P.R. China

Received 25 January 2000 / Accepted 17 August 2000

Abstract. Based on the three dimensional outer magnetosphere model of pulsars proposed by Cheng, Ruderman and Zhang, we calculate the light curves and spectra of the Crab-like pulsars: PSR B0540-69 and PSR B1509-58. In this model, thermal photon emission from the entire stellar surface is due to the bombardment of the backflow charged particles from the outer gap and cyclotron resonance scattering (Cheng & Zhang 1999). Non-thermal photons are emitted by $e^{\pm}$ pairs produced by backflow charged particles from the outer gap through a synchrotron radiation mechanism near the stellar surface and in a finite region just above the outer gap through a synchrotron self-Compton mechanism. For PSR B1509-58, when the magnetic inclination and viewing angle are 60° and 75° respectively, the photon emission region has a mean thickness of $\sim 0.11R_L$, where R_L is the radius of the light cylinder. The expected broad single pulse in optical, X-ray and γ-ray energy bands are comparable with the observed light curves with a correct phase off-set with respect to the radio pulse, and the model spectrum is consistent with the observed spectrum. For PSR B0540-69, the calculated mean thickness of the photon emission region is $\sim 0.21R_L$ and the model light curve and spectrum are similar to the observed data if the magnetic inclination and viewing angle are 50° and 76° respectively.

Key words: stars: pulsars: individual: PSR B0540-69 – stars: pulsars: individual: PSR B1509-58 – gamma rays: theory – X-rays: stars

1. Introduction

It is commonly accepted that a three dimensional outer gap model is necessary in order to explain the observed light curves and phase-resolved spectra of γ-ray pulsars. Outer gaps, which are powerful acceleration regions, can form in the vicinity of a "null charge surface" ($\mathbf{\Omega} \cdot \mathbf{B} = 0$) (Holloway 1973; Cheng et al. 1976) because the charge carriers on each side of the null charge surface have opposite charges. Current passing through this surface removes charge in the vicinity of the null surface and a charge vacuum forms there. Cheng et al. (1986a, 1986b, hereafter CHR I and CHR II) proposed an outer gap model to explain the observed data of the Crab and Vela pulsars (also see Ho 1989). Their model assumed that the radiation regions are thin in the longitudinal direction. The double peak structure in the pulse profile predicted by the model results from two topologically disconnected outer gaps, each of which is associated with different magnetic poles. However, Romani and coworkers (Chiang & Romani 1992, 1994; Romani & Yadigaroglu 1995; Romani 1996) have shown that one outer gap with only outgoing current can itself produce a broad, irregularly-shaped emission beam which is particularly dense near the edge, so that two γ-ray peaks would be observed when the line of sight from the Earth crosses these enhanced γ-ray beam regions; the inner region of the beam provides a significant amount of emission between the peaks. Recently, Cheng et al. (2000) (hereafter CRZ) have re-considered conditions in the three dimensional magnetosphere using various physical processes to determine the three-dimensional geometry of the outer gap (including pair production which depends sensitively on the local electric field, the local radius of curvature, surface field structure, and reflection of $e^{\pm}$ pairs because of mirroring and resonant scattering). They have shown that two outer gaps and both outgoing and incoming currents are, in principle, allowed, but that outgoing currents dominate the emitted radiation intensities. The observed features of the Crab pulsar can be well explained by this model.

Based on the outer gap model of high-energy radiation from the pulsars which we have proposed (Zhang & Cheng 1997; see also Cheng et al. 1998), we (Cheng & Zhang 1999) have studied in detail the X-ray production near or on the pulsar surface due to backflow high-energy electrons/positrons from the outer gaps. In particular, the soft thermal X-ray spectra of Geminga and PSR B1055-52 are consistent with this backflow current heating model. Here we report the X-ray emissions in the three dimensional magnetosphere, and give X-ray light-curves and spectra, which would be tested by measurements by newly launched satellites, e.g. XMM, Chandra etc.

For the known γ-ray pulsars, two pulsars may be Crab-like pulsars: PSR B0540-69 and PSR B1509-58. PSR B0540-69 in the Large Magellanic Cloud (LMC) is one of the youngest and most luminous rotation-powered pulsars, its period and period derivative are 50 ms and 4.8×10^{-13} s s^{-1}, which implies a characteristic age of $\tau = 1.5 \times 10^3$ yr. PSR B1509-58 is a

Send offprint requests to: L. Zhang

pulsar with a period of 150 ms and period derivative of 1.5×10^{-12} s s^{-1}. Its characteristic age of $\tau = 1.6 \times 10^3$ yr makes it the second youngest known pulsar behind only the Crab pulsar. In Sect. 2, we describe an outer gap model of Crab-like pulsars, and then apply this model in Sect. 3 to explain the light curves and spectra of PSR B1509-58 and PSR B0540-69. Our results are summarized in Sect. 4.

2. The three dimensional outer gap model of crab-like pulsars

2.1. The structure of the outer gap

CRZ have proposed a three dimensional outer gap model for rotation-powered pulsars with a thin outer gap. They successfully applied this model to the Crab pulsar. In this model, polar cap shape is determined first because it defines the boundary of the open volume at the stellar surface. Because the outer gaps are within the open volume, the open volume is divided into many parts, in which the shape of each part at the stellar surface is the same as the shape of the polar cap but with a smaller size. If the coordinate values (x_0, y_0, z_0) represent the values of the last closed field lines at the stellar surface, then the coordinate values (x_0', y_0', z_0') for different parts can be determined by using $x_0' = a_1 x_0$, $y_0' = a_1 y_0$ and $z_0' = (1 - (x_0'^2 + y_0'^2))^{1/2}$ and by changing a_1. It should be pointed out that $a_1 = 1$ corresponds to the last closed field line and $a_1 < 1$ to open field lines in the magnetosphere. Once the polar cap shape is given, which depends on pulsar parameters such as period, magnetic field and the magnetic inclination angle, the structure of an outer gap can be determined as follows:

According to CRZ, the azimuthal extension of the outer gap ($\Delta\Phi$) is finite and is determined by the local pair production condition. Two mechanisms may be responsible for it. For an oblique dipole, the radius of the inner boundary of the outer gap ($r_{in}(\phi)$)(the intersection of the null charge surface with the last closed field lines) changes with azimuthal angle (ϕ). If we define $\phi = 0$ at the (x, z) plane, then $r_{in}(\phi)$ increases from $\phi = 0^\circ$ to $\phi = 180^\circ$, and decreases from $\phi = 180^\circ$ to $\phi = 360^\circ$. In the ($\mathbf{\Omega}$, μ) plane, four gaps (two long gaps labeled gaps 1 and 2 and two short gaps labeled gaps 3 and 4) exist in the outer magnetosphere (CHR I). However, it has been shown (Halpern & Ruderman 1993; Zhang & Cheng 1997, hereafter ZC; Zhang & Cheng 1998; Cheng et al. 1998; Wang et al. 1998) that half charged particles produced in gap 1 and gap 2 will move toward the star and lose their energy via curvature radiation. Part of the high energy curvature photons will be converted into secondary $e^\pm$ pairs in the field lines which connect to gap 3 and 4 via either photon-photon pair creation or magnetic pair production. Part of incoming secondary pairs created in low magnetic field regions can be reflected back and enter gaps 3 and 4 (Ho 1986). Those secondary pairs created in strong magnetic field regions will lose their energies via synchrotron radiation but some of these lower energy secondary pairs will be reflected back by the resonant X-ray scattering near the stellar surface (Wang et al. 1998) and also enter gap 3 and gap 4. Therefore, the reflected outgoing $e^\pm$ pairs can enter the gaps 3 and 4 to quench them. In this case the extension along the azimuthal direction is about 180°, corresponding to the maximum value of the inner boundary of the outer gap r_{in}' where the null charge surface intercepts the light cylinder. In this case, if the magnetic inclination angle is not less than $\sim 20^\circ$, we find that the azimuthal extension of the outer gap is about 180°. Another mechanism is that the extensions of the outer gap along both azimuthal and radial directions are limited by local pair production processes. The pair production per unit length inside the outer gap is a decreasing function of r. According to Cheng et al. (1986), $E_{||} \propto r^{-1/2}$ for the thin outer gap (e.g. the Crab pulsar), which gives $E_\gamma(r) \propto r^{-1/8}$ after using the large r limit $s(r) = (rR_L)^{1/2}$. Since E_γ is only weakly dependent on r, we assume $\sigma_{\gamma\gamma} \approx const$. The local pair production per unit length is

$$N_{e^\pm}(r) = (1 - e^{-\tau_{\gamma\gamma}}) N_\gamma(r) \approx \tau_{\gamma\gamma} N_\gamma(r) \quad , \tag{1}$$

where $\tau_{\gamma\gamma} = n_X(r)\sigma_{\gamma\gamma} l(r)$ is the local optical depth, $n_X = R^2 T_s^4 \sigma / r^2 k T_s c$ is the X-ray number density at r, $l(r) \approx (2s(r)f(r)R_L)^{1/2}$ is the local optical path, $N_\gamma = eE_{||}(r)/E_\gamma(r)$ is the number of curvature photons emitted at r per e^+/e^- per unit length, and $f(r) = h(r)/R_L$ is the local vertical extension of the gap. Since $B(r)h^2(r)$ is a constant, which gives $f(r) \propto r^{3/2}$, and $f_0 \sim f(R_L/2)$ which is the average size of the outer gap and is given by (Zhang & Cheng 1997, hereafter ZC)

$$f_0 \approx 5.5 P^{26/21} B_{12}^{-4/7} \left(\frac{\Delta\Phi}{2\pi}\right)^{1/7} \quad . \tag{2}$$

Therefore

$$N_{e^\pm}(r) \propto r^{-11/8} \quad . \tag{3}$$

We see that most pairs are produced near the null surface where $r = r_{in}$. We estimate that the pair production will take place mainly in the range $r_{in} \le r \le r_{lim}'$ where r_{lim}' is estimated as $r_{lim}' N_{e^\pm}(r_{lim}')/r_{in} N_{e^\pm}(r_{in}) \sim (r_{lim}'/r_{in})^{-3/8} \sim 1/2$, which gives $r_{lim}' \sim 6 r_{in}$. This limits pair production both along the field lines and in transverse directions, and gives $\Delta\Phi(r_{lim}')$ which depends on the magnetic inclination angle. Therefore, the azimuthal extension of the outer gap is

$$\Delta\Phi \approx min(180^\circ, \Delta\Phi(r_{lim}')) \tag{4}$$

and the pair production region inside the outer gap is in the region from r_{in} to r_{lim}, where

$$r_{lim} = min(r_{in}', r_{lim}') \quad . \tag{5}$$

Within the pair production regions, outgoing and incoming directions for particle flows are allowed. For $r > r_{lim}$ only outgoing current is possible. It should be pointed out that four gaps may be active or inactive for an aligned dipole.

We want to point out that the soft photons in the Crab-like pulsars will be non-thermal photons which are produced by the synchrotron radiation by the secondary pairs (CHR II). CHR II estimated that the fractional size of the outer gap for the crab pulsar is ~ 0.05 by taking into account the effect of the synchrotron photons, while Eq. (2) gives 0.04. Since this estimate is

so close, we will use Eq. (2) as a rough approximation for estimating f_0. In fact, in the three dimensional case, such estimate of the fractional height of the outer gap including secondary synchrotron photons becomes very difficult because both high energy photons and the soft target flux are produced by the gaps themselves (Romani 1996).

Briefly, for Crab-like pulsars, there may be two outer gaps in the outer magnetosphere. The structure of an outer gap is as follow: (i) the fractional height of the outer gap is given by f_0, (ii) the azimuthal extension is about $\sim 160^\circ$ and (iii) the radial extension is from r_{in} to R_L with small region ($r_{lim} - r_{in}$) of photon-photon pair production.

2.2. Photon emission processes and patterns

Because of the backflow of high-energy electrons/positrons from the outer gap, thermal and non-thermal X-rays will be produced near or on the pulsar surface (ZC, Cheng et al. 1998; Cheng & Zhang 1999). Briefly, according to ZC, thermal hard X-rays from the stellar surface result from the bombardment of the return current. Most of these X-rays will be reflected back to the stellar surface due to resonant cyclotron scattering by the $e^{\pm}$ plasma screen on the strong magnetic field lines. Finally soft X-rays from the entire stellar surface will be emitted with a typical temperature $T_s \sim 3.8 \times 10^5 f_0^{1/4} P^{-5/12} B_{12}^{1/4}$ K. The soft X-ray spectrum can be written as (ZC)

$$\frac{d\dot{N}_X^{thermal}}{dE_X} = A_s \frac{E_X/mc^2)^2}{e^{E_X/kT_s} - 1} \tag{6}$$

where $A_s = (15/\pi)^4[(mc^2)^2/(kT_s)^4]L_X$ and $L_X \approx 3.3 \times 10^{31} f_0 B_{12} P^{-5/3}$ ergs s^{-1}. On the other hand, primary electrons/positrons leaving the outer gap emit curvature photons with a typical energy E_{cur}, which is

$$E_{cur}(r) \approx 2.3 \cdot 10^9 f_0^{3/2} B_{12}^{3/4} P^{-7/4} \left(\frac{r}{R_L}\right)^{-1/8} \quad \text{eV} . \tag{7}$$

These high energy γ-rays will be converted into secondary $e^{\pm}$ pairs by a magnetic-pair production process at a position

$$\frac{r_s}{R} \approx 0.55 B_{12}^{1/3} \left(\frac{E_{cur}}{mc^2}\right)^{1/3} \quad . \tag{8}$$

Subsequently, these $e^{\pm}$ pairs at r_s lose their energies rapidly via synchrotron radiation with typical energy

$$E'_{syn} = \frac{3}{2}\left(\frac{E_{cur}}{2mc^2}\right)^2 \hbar \frac{eB(r_s)}{mc} = \frac{E_{cur}}{20} \tag{9}$$

and the spectral index $\beta_i = 1.5$. These synchrotron photons will be further converted into $e^{\pm}$ pairs if their energies are large enough. Therefore, the non-thermal X-rays are produced by a cascade process (the detail see Cheng et al. 1998). The luminosity of these non-thermal X-rays is (Cheng et al. 1998)

$$L_X^n \approx 5.5 \times 10^{-4} \left(\frac{\tan\chi}{\tan 55^\circ}\right)^4 B_{12}^{0.13} (P/0.1)^{0.80} L_{sd} \tag{10}$$

with $L_{sd} \approx 3.8 \times 10^{31} B_{12}^2 P^{-4}$ ergs/s. If r_f is the position at which the cascade stops, then the minimum and maximum energies of these non-thermal X-rays are

$$E_{X,min} = \hbar(eB(r_f)/mc) \approx 1.1 \times 10^4 B_{12} (r_f/R)^{-3} \quad \text{eV} \tag{11}$$

and

$$E_{X,max} = \left(\frac{1}{20}\right)^{n_f} E'_{syn} \tag{12}$$

respectively, where n_f is the generation number. Note that $r_f/R = (1/20)^{n_f/3}(r_s/R)$. Below $E_{X,min}$, the spectrum has a break with spectral index $-1/3$. Therefore the spectrum of these non-thermal X-rays is given by

$$\frac{d\dot{N}_X^n}{dE_X} = A_n \left(\frac{E_X}{\text{keV}}\right)^{-\beta_f} \quad \text{for } E_{X,min} \le E_X \le E_{X,max} \tag{13}$$

and

$$\frac{d\dot{N}_X^n}{dE_X} = A_n E_{x,min}^{-\beta_f+1/3} \left(\frac{E_X}{\text{keV}}\right)^{-1/3} \quad \text{for } E_X < E_{X,min}, \tag{14}$$

where

$$A_n \approx \frac{(2-\beta_f)}{E_{x,max}^{2-\beta_f} - E_{X,min}^{2-\beta_f}} \frac{L_X^n}{(\text{keV})^2} \quad . \tag{15}$$

The spectral index (β_f) depends on the cascade generation. Here, we assume that there are two generation in this cascade, so $\beta_f = 1.875$.

CRZ have argued that most curvature photons emitted from the accelerator will become secondary pairs outside the gap in Crab-like pulsars, where the local magnetic field in the outer gap accelerator is sufficiently strong to give KeV synchrotron radiation. These secondary pairs will boost a fraction of the synchrotron photons to high energy γ-rays through inverse Compton scattering. Therefore, for Crab-like pulsars, photon emission comes from the emission region above the outer gap through a synchrotron self-Compton mechanism. Because those photons emitted into a given pulse phase come from different positions of the outer gap, and curvature radiation, synchrotron radiation and inverse Compton scattering depend on local quantities, e.g. curvature radius, $E_{||}$, B, n_{ph} etc., so it is likely that the radiation spectrum varies with phase. Here we assume that the distribution of secondary electrons/positrons at steady state is

$$\frac{d^2N}{dE_e} = N_0(r) E_e^{-p} \quad \text{for} \quad E_{min} \le E_e \le E_{max} \quad , \tag{16}$$

where $N_0(r) \sim (l_{cur} n_{GJ}/E_{cur})$, $l_{cur}(r) = eE_{||}(r)c$ is the local power in curvature radiation produced by a single e^+/e^-, n_{GJ} is the local Goldreich-Julian number density. E_{cur} is is given by Eq. (7), p is the spectral index. $E_{min} \sim mc^2$ and $E_{max} \approx E_{cur}/2$ are the minimum and maximum energy of the secondary pairs respectively.

For photon emission from the emission region above the outer gap, it is important to estimate the thickness of the emission region. CRZ have argued that the lower-energy photons produced by the synchrotron radiation of the secondary pairs outside the outer gap cannot enter the outer gap itself, but they can collide with the high-energy curvature photons at an angle $\sim f_0$. The number density of these low energy photons is $n_X \sim L_{gap}/\langle r\rangle^2 cE_X$, where $L_{gap} \sim f_0^3 L_{sd}$ and $L_{sd} \approx 3.85\times10^{31}P^{-4}B^2 12$ ergs/s. Therefore, the mean free path in which pairs are produced outside the outer gap is $\lambda_{X\gamma} \sim (n_X\sigma_p)^{-1}$, where $\sigma_p \sim \sigma_T/3$ is the pair production cross section and σ_T is the Thompson cross section. Using $\langle r\rangle \sim R_L/2$ and $E_X \approx (mc^2)^2/(f_0E_{cur})$, we have

$$\lambda_{X\gamma} \sim 1.7\times10^{-3}f_0^{-4}\left(\frac{P}{0.1\mathrm{s}}\right)^5\left(\frac{E_{cur}}{10\mathrm{GeV}}\right)^{-1}B_{12}^{-2}R_L \ . \quad (17)$$

The corresponding pitch angle is estimated by $\sin\beta(R_L/2) \sim \lambda_{X\gamma}/(R_L/2)$. The photon spectrum of the synchrotron radiation of these secondary pairs is

$$F_{syn}(E_\gamma, r) = \frac{3^{1/2}e^3B(r)\sin\beta(r)}{mc^2h}\frac{1}{E_\gamma} \int_{E_{min}}^{E_{max}}\left(\frac{dN(r)}{dE_e}\right)F(x)dE_e \quad , \quad (18)$$

where $x = E_\gamma/E_{syn}$.

$$E_{syn}(r) = \frac{3}{2}\left(\frac{E_e}{mc^2}\right)^2\frac{\hbar eB(r)\sin\beta(r)}{mc} \quad (19)$$

is the typical energy and $F(x) = x\int_x^\infty K_{5/3}(y)dy$, where $K_{5/3}(y)$ is the modified Bessel function of order 5/3. In Eq. (19), $\beta(r)$ is the local pitch angle and $\sin\beta(r) \sim (r/R_L)^{1/2}\sin\beta(R_L)$ (CRZ). Similarly, the spectrum of inverse Compton scattered photons in volume $\Delta V(r)$ is

$$F_{ICS}(E_\gamma, r) = \int_{E_{min}}^{E_{max}}\left(\frac{dN(r)}{dE_e}\right)\left(\frac{d^2N_{ICS}(r)}{dE_\gamma dt}\right)dE_e \ , \quad (20)$$

where

$$\frac{d^2N(r)_{ICS}}{dE_\gamma dt} = \int_{\epsilon_1}^{\epsilon_2} n_{syn}(\epsilon, r)F(\epsilon, E_\gamma, E_e)d\epsilon \quad , \quad (21)$$

and

$$F(\epsilon, E_\gamma, E_e) = \frac{3\sigma_T c}{4(E_e/mc^2)^2}\frac{1}{\epsilon}[2q\ln q + (1+2q)(1-q) + \frac{(\Gamma q)^2(1-q)}{2(1+\Gamma q)}] \quad , \quad (22)$$

with $\Gamma = 4\epsilon(E_e/mc^2)/mc^2$, $q = E_1/\Gamma(1-E_1)$ with $E_1 = E_\gamma/E_e$ and $1/4(E_e/mc^2) < q < 1$. The number density of the synchrotron photons with energy ϵ is

$$n_{syn}(\epsilon, r) = \frac{F_{syn}(\epsilon)}{cr^2\Delta\Omega} \quad , \quad (23)$$

where F_{syn} is the calculated synchrotron radiation flux, and $\Delta\Omega \sim 2\pi(1-\cos\beta(r))$ is the usual beam solid angle.

We now describe the photon emission patterns. We assume that relativistic charged particles in the open zone radiate along the magnetic field lines in the corotating frame, then we project photon emission on (ζ, Φ) plane, where ζ is the polar angle from the rotation axis and Φ is the phase angle of rotation of the star. In the calculations, we have taken the effects of travel time and aberration into account, and chosen $\Phi = 0$ for emission in the (x, z) plane from the center of the star. Therefore, for a given magnetic inclination angle, we can calculate the photon emission patterns of a given pulsar on the sky, and then can obtain the light curve for a specific viewing angle (for details see Romani 1996; CRZ).

3. Model results

We apply this three dimensional outer gap model to Crab-like pulsars: PSR B1509-58 and PSR B0540-69, and model the light curves and the spectra of optical, X-rays and γ-rays from these two pulsars. For a Crab-like pulsar with a given magnetic inclination angle, our calculation procedure is as follow.

For the thermal X-ray emission produced by the backflow of high-energy electrons/positrons near the stellar surface, the thermal X-rays are assumed to be isotropic, while, for the non-thermal X-rays, as an approximation, we trace the magnetic field lines from the position r_s (see Eq. (8)) to the position $r_\perp$, which denotes the normal intercept from the center of the star to the tangent to the field line at the point (x, y, z) of the outer gap where the photons are created:

$$r_\perp = \left(r^2 - \frac{(x\dot{x}+y\dot{y}+z\dot{z})^2}{\dot{x}^2+\dot{y}^2+\dot{z}^2}\right)^{1/2} \quad . \quad (24)$$

The photons with $r_\perp > R$ cannot collide with the stellar surface.

For the non-thermal photon emission above the outer gap, we trace the magnetic field lines by changing a_1 for a given f_0 (which can be approximated by Eq. 2), and require that the interval (in units of R_L) between the field line and the last closed field line (corresponding $a_1 = 1$) at radius of $R_L/2$ equal f_0. We thereby find a value of a_1 which approximately defines the upper boundary of the outer gap (we label it as a_1^u). We then trace the magnetic field lines for a different a_1 and find the value of a_1 (we label it as a_1^r) where the interval between the field lines with a_1^r and the field lines with $a_1 = a_1^u$ at radius of $R_L/2$ equals $\sim \lambda_{X\gamma}/R_L$, where $\lambda_{X\gamma}$ is given by Eq. (17). After estimating a_1^u and a_1^r, we calculate the emission pattern of non-thermal photons produced in the emission region above the outer gap and the variation of radial distances with pulse phase in this emission region for a given viewing angle. Finally we calculate the light curve and spectrum of this Crab-like pulsar. In our calculation, we assume that the spectral index of the secondary pairs is 2 (i.e. we have approximated the curvature radiation spectrum as a δ function). Although $\sin\beta(R_L)$ can be roughly estimated by using $\sin\beta(R_L) \sim \sqrt{2}\sin\beta(R_L/2)$ with $\sin\beta(R_L/2) \sim \lambda_{X\gamma}/(R_L/2)$, here we use it as a parameter.

3.1. PSR B1509-58

PSR B1509-58 is believed to be a Crab-like pulsar because its parameter B/P^2 is very close to that of the Crab pulsar. PSR B1509-58 was discovered as an X-ray pulsar (Seward & Harnden 1982). Its pulsed emission has been detected at radio frequencies (Manchester et al. 1982), soft X-rays (Becker & Trümper 1997), hard X-rays (Kawai et al. 1993; Matz et al. 1994; Rots et al. 1998), low energy γ-rays (e.g. Ulmer et al. 1993) and medium energy γ-rays (Carraminana et al. 1995, 1997; Kuiper et al. 1999). The observed data indicate that (i) the light curves of hard X-rays and low energy γ-rays have a broad single peak, (ii) the X-ray pulse lags the radio pulse by about 0.27 ± 0.01 period, with no evidence for any energy dependence in the range 2–100 keV (Rots et al. 1998), (iii) the low energy γ-ray pulse lags the radio pulse by 0.32 ± 0.02 (Ulmer et al. 1993) or ~ 0.3 periods (Rots et al. 1998), and (iv) medium energy γ-ray pulse lags the radio pulse by 0.30 ± 0.06 period (Carraminana et al. 1997). Rots et al. (1998) pointed out that the change in phase lags of X-rays and low energy γ-rays can be due to a gradual change in the dispersion measure. According to our model, hard X-rays and low energy γ-rays have the same origin, i.e. they are produced by synchrotron self-Compton radiation of secondary $e^{\pm}$ pairs of the outer gap. Therefore, the phase offsets of hard X-rays and low energy X-rays with respect to the radio pulse are the same. However, a small phase lag between X-rays and low energy γ-rays is still possible because the emission regions of X-ray and γ-rays is very thick. Each layer of the emission can contribute to X-rays and γ-rays differently. For example, synchrotron radiation from the regions near the light cylinder radius contribute fewer gamma-rays than do the regions near the star. A more detailed study on energy-dependent light curves will be presented elsewhere.

We consider the light curve and spectra of PSR B1509-58 using the three dimensional outer gap model described in Sect. 2. In order to determine the emission pattern, we need to know the magnetic inclination angle and viewing angle. Unfortunately, we cannot obtain any constraints on the two angles from radio observation. Therefore, we estimate these two angles as follows: (i) the viewing angle must cross the radio beam which is $\sim 6.3/\sqrt{P} \sim 16.3^\circ$ for PSR B1509-58 and (ii) the phase offset with respect to radio pulse is ~ 0.3 and the pulse is a single broad peak. We have tried to calculate various angles and found that model light curve with a magnetic inclination angle of about 60° and a viewing angle of 75° can compare with the observed light curves. These results are consistent with those estimated by Romani & Yadigaroglu (1995). After determining the inclination and viewing angles, we follow the calculation procedure described above to describe the emission patterns. For non-thermal photon emission near stellar surface, we estimate the pair production position r_s using Eq. (8), and follow the photon traces along the magnetic field lines inwards to the positions given by Eq. (24). The emission patterns are shown in panel A of Fig. 1. When we consider the emission patterns of the non-thermal photons above the outer gap, we find that $a_1^u \sim 0.90$ for $f_0 \sim 0.12$ (which is estimated by using Eq. (2)) and $a_1^r \sim 0.62$ for $\lambda_{X\gamma}(R_L/2) \sim 0.11 R_L$ (which is estimated by using Eq. (17)). Therefore, the non-thermal radiation above the outer gap is produced in the emission region from $a_1^u = 0.90$ to $a_1^r = 0.62$. The emission pattern is shown in panel A of Fig. 1 (the radio caps are also shown). Furthermore, we estimate the radial distances of the emission region above the outer gap which is a function of pulse phase (shown in panel B of Fig. 1). Furthermore, we calculate the intensity of non-thermal photons from the emission region which is function of the pulse phase. Therefore, we obtain the light curves of the Crab-like pulsars once the inclination angle, viewing angle and the thickness of photon emission region are given. The light curves corresponding to the emission pattern of panel A of Fig. 1 are shown in panel C, in which the radio pulse is schematic. We assume that the radio emission comes from the polar cap, so its phase is zero. As a comparison, the dashed histogram in the panel C of Fig. 1 represents the observed pulse profile data for the X-ray band of 16 -32 KeV measured by RXTE (Rots et al. 1998), where we take the value at pulse phase 0° as zero. In panel C of Fig. 1, we schematically show the light curve of the thermal photons coming from the entire stellar surface.

Using the parameters given above, we calculate the radiation spectrum from PSR B1509-58. We divided the phase into three bins: $\sim -15^\circ \leq \phi \leq \sim 50^\circ$, $\sim 60^\circ \leq \phi \leq \sim 180^\circ$, and $\sim 180^\circ \leq \phi \leq \sim 270^\circ$. In the phase bin from 180° to 270°, the photon emission is dominated by thermal photons coming from the stellar surface, with the expected thermal photon spectrum as shown in Fig. 2, where isotropic emission is assumed. The spectrum of the non-thermal photons in the phase bin from $\sim -15^\circ$ to 50° is shown in Fig. 3, where the photons are produced near the stellar surface due to the cascade process and the beaming solid angle is assumed to be 1 sr. The non-thermal photon emission above the outer gap ranges from $\sim 60^\circ$ to $\sim 180^\circ$. Its phase-resolved spectrum is shown in Fig. 4, where the expected spectra for $\sin\beta(R_L) = 0.7$, 0.5 and 0.3 respectively are shown.

The comparison of the phase-averaged spectrum with the observed one is shown in Fig. 5. Up to now, GINGA has observed X-ray spectrum with a spectral index of 1.3 ± 0.05 in the (2-60) KeV energy range (Kawai et al. 1993). In the medium γ-ray energy range, COMPTEL showed a detection in the energy range from 0.75 MeV to 30 MeV (Kuiper et al. 1999). At the high energy range, PSR B1509-58 was not detected by EGRET. Here we use the data compiled by Thompson et al. (1999), ROSAT data (Becker & Trümper 1997), ASCA data (Saito 1998) and new COMPTEL data (Kuiper et al. 1999). In our calculation of the phase-averaged spectrum, we determined the relative intensities of three components (the soft X-rays, non-thermal X-rays produced near the stellar surface and non-thermal photons produced above the outer gap), then used the expected spectrum to fit the observed data by adjusting the beaming solid angle, which is 3.9 sr for $\sin\beta(R_L) = 0.5(r/R_L)^{1/2}$. It can be seen that there is a general agreement between the expected result and the observed spectrum. In Fig. 5, the three components are also shown respectively.

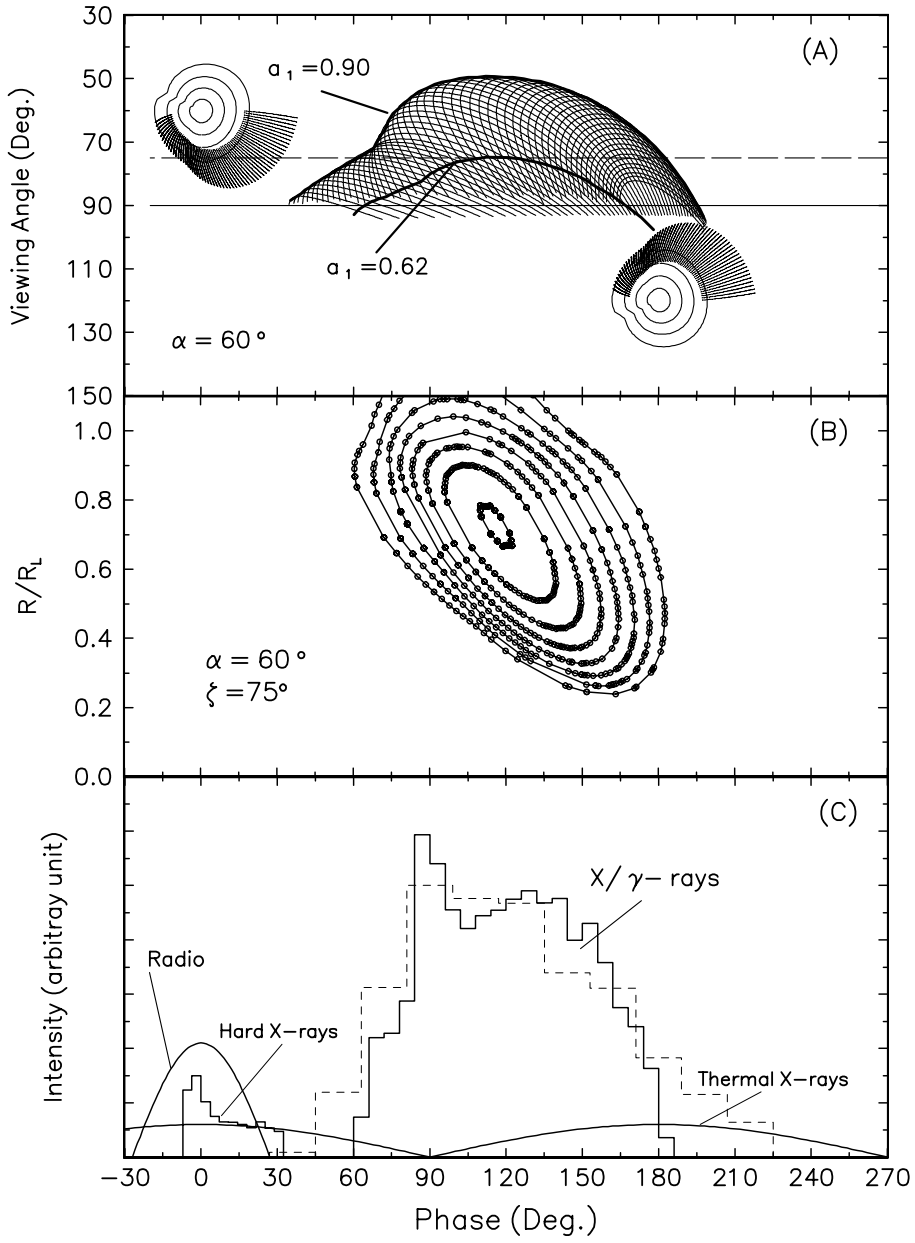

Fig. 1a–c. Emission projection onto the (ζ,Φ) plane and pulse profile for PSR B1509-58 ($\alpha = 60^\circ$). Panel A: Photon emission from the pulsar as a function of phase, the solid curves indicate outward photon emission from the emission region above a single outer gap. The tiny-solid curves represents inward and outward non-thermal photon emission from the region near the stellar surface. The observed lines of sight at $\zeta = 75^\circ$ and $\zeta = 90^\circ$ (dashed and solid lines), and both polar caps (contours) are shown. Panel B: The variation of radial distance with pulse phase for the thickness of the emission region of $\sim 0.11R_L$. The curves represent trajectories for $a_1 =$ 0.90, 0.86, 0.82, 0.78, 0.74, 0.70, 0.66 and 0.62. Panel C: Pulse profile for PSR B1509-58. The model X-ray/γ-ray pulse at $\zeta = 75^\circ$ is shown. For comparison with the observed data, we have shown the observed pulse profile data for the X-ray band of 16–32 KeV measured by RXTE (dashed histogram) (Rots et al. 1998), where we assume that the value at pulse phase 0° is zero.

3.2. PSR B0540-69

PSR B0540-69 was discovered in the soft X-ray band by the Einstein X-ray Observatory (Seward et al. 1984). Optical and radio pulses were detected by Middleditch & Pennypacker (1985) and Manchester et al. (1993), respectively. Moreover, X-ray pulses from PSR B0540-69 have been detected by various X-ray detectors such as GINGA (Nagase et al. 1990; Deeter et al. 1999), ROSAT (Finley et al. 1993; Eikenberry et al. 1998), BeppoSAX (Mineo et al. 1999), and Chandra (Gotthelf & Wang 2000), but pulses of γ-rays were not detected by OSSE, COMPTEL and EGRET and only upper limits in those energy ranges are available. All these observations indicate that (i) PSR B0540-69 has a single broad pulse profile in the radio band, and (ii) there is a close alignment between the optical and X-ray pulse profiles. Although the radio pulse was detected, the pulse offset of X-rays with respect to the radio pulse has not been determined.

PSR B0540-69 is one of the youngest rotation-powered pulsars. Its energy and age have been found to be similar to those of the Crab pulsar, but with different pulse profiles. In fact, X-ray/γ-ray emission from the Crab pulsar indicate two peaks with a phase separation of ~ 0.4. Since (i) it has a broad X-ray pulse with a width of about 0.45 phase which is similar to that of PSR B1509-58, and (ii) we observe both radio and X-ray pulses (the radio beam is $6.3^\circ P^{-1/2} \sim 28^\circ$), we expect that the viewing angle is far away from $\xi = 90^\circ$ and the magnetic inclination is not less than $\sim 40^\circ$. However, because the phase offset of X-rays with respect to the radio pulse is not clear, it is difficult to estimate the values of the viewing angle and the magnetic inclination. We have chosen different magnetic incli-

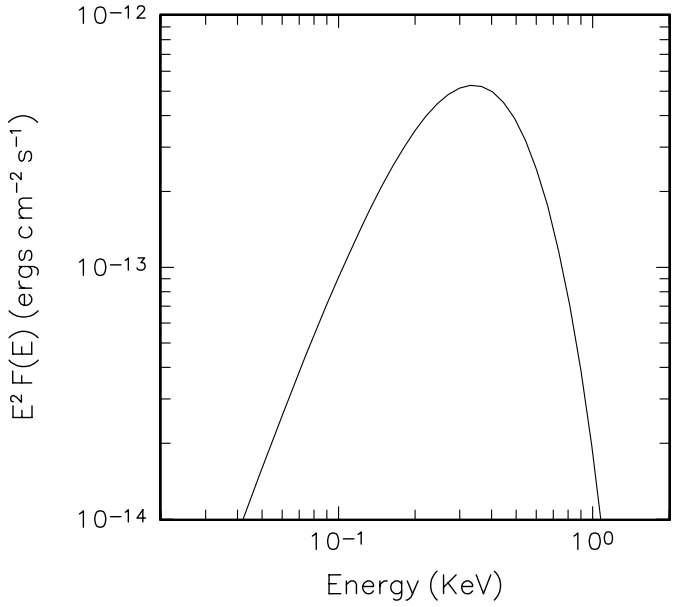

Fig. 2. Phase-resolved spectrum of PSR B1509-58 in the phase bin from $\sim 180^\circ$ to $\sim 270^\circ$. The photon emission in this phase bin is dominated by the thermal photons from the stellar surface.

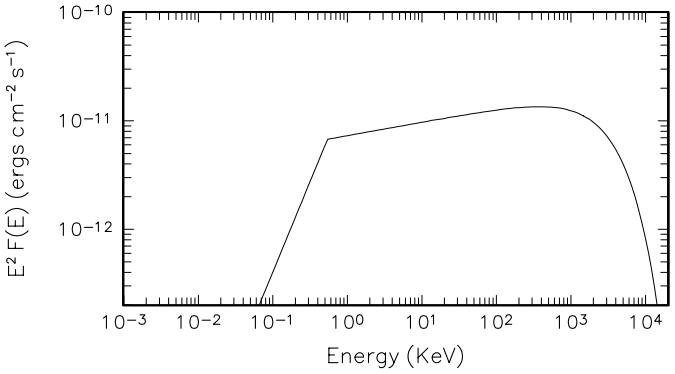

Fig. 3. Phase-resolved spectrum of PSR B1509-58 in the phase bin from $\sim -15^\circ$ to $\sim 50^\circ$. The photon emission in this phase bin is dominated by the non-thermal photons produced near the stellar surface. The beaming solid angle is assumed to be 1 sr.

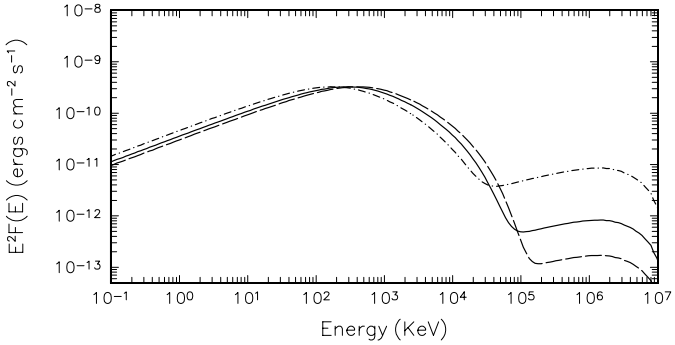

Fig. 4. Phase-resolved spectrum of PSR B1509-58 in the phase bin from $\sim 60^\circ$ to $\sim 180^\circ$. The photon emission in this phase bin is dominated by the non-thermal photons produced above the outer gap. The solid, dashed and dot-dashed curves represent model results for $\sin(\beta(R_L)) = 0.3$, 0.5 and 0.7 respectively. The beaming solid angle is assumed to be 1 sr.

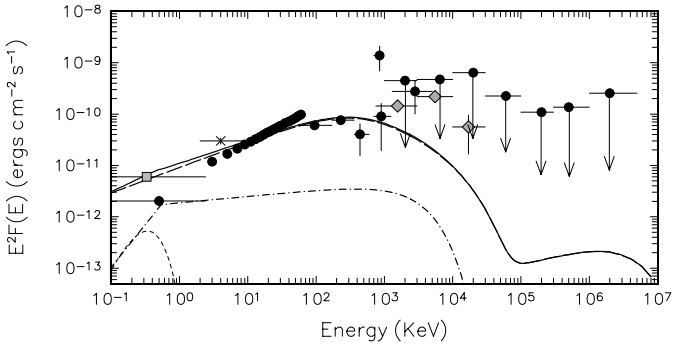

Fig. 5. The comparison of model spectra with the observed data for PSR B1509-58. The solid curve represents model result for $\sin(\beta(R_L)) = 0.5$. We have used the observed data (solid circles) compiled by Thompson et al. (1999) which include X-ray data (Seward et al. 1984; Kawai et al. 1993) and gamma-ray data (Matz et al. 1994; Nel et al. 1996), ROSAT data (box) (Becker & Trümper 1997), ASCA data (cross) (Saito 1998) and COMPTEL data (solid diamonds) (Kuiper et al. 1999).

nation and viewing angles to calculate the pulse profiles with the constraints that (i) viewing angle must cross the radio beam and (ii) the X-ray pulse profile must have a broad shape. Because the thickness of the emission region above the outer gap is limited by Eq. (17), a broad X-ray pulse profile will have the result that the viewing angle will not cross the radio beam for small magnetic inclination angles (say less than 45°). Furthermore, the pulse width is too small compared to the observed data for a large inclination angle (larger than 60°). Therefore, we chose a magnetic inclination and viewing angle of 50° and 76° respectively. Because of the large r_{in} for small magnetic inclinations, the extension of the outer gap is about 180° and the corresponding r_{lim} is determined by the value of r_{in} at $\phi \sim 180^\circ$. For PSR B0540-69, we have $f_0 \sim 0.05$ and $\lambda_{X\gamma} \sim 0.21 R_L$ which give $a_1^u \sim 0.95$ and $a_1^r \sim 0.71$. According to our calculation described above, the emission patterns of the non-thermal photons due to the backflow of high-energy electrons/positrons from the outer gap is shown by the dashed curves in panel A of Fig. 6. The non-thermal photon emission pattern of the emission region from a_1^u to a_1^r in the (ζ, Φ) plane and radio caps are shown in panel A of Fig. 6, where outgoing and incoming emission patterns are represented by solid curves and dashed curves respectively. Then we calculate the radial distances of the emission region, which vary with the pulse phase. In panel B of Fig. 6, we show such a variation of the radial distance of the emission region with pulse phase. Finally, we calculate photon intensity from the emission region which is a function of the pulse phase and show the light curves corresponding to the emission pattern in panel C of Fig. 6, where we assume that the radio emission comes from the polar cap, so that its phase is zero and the radio pulse is schematic. As mentioned above, because the pulse offset of X-rays with respect to the radio pulse is not known and the X-ray background has not been well determined, it is not easy to compare our results with the observed pulse profile.

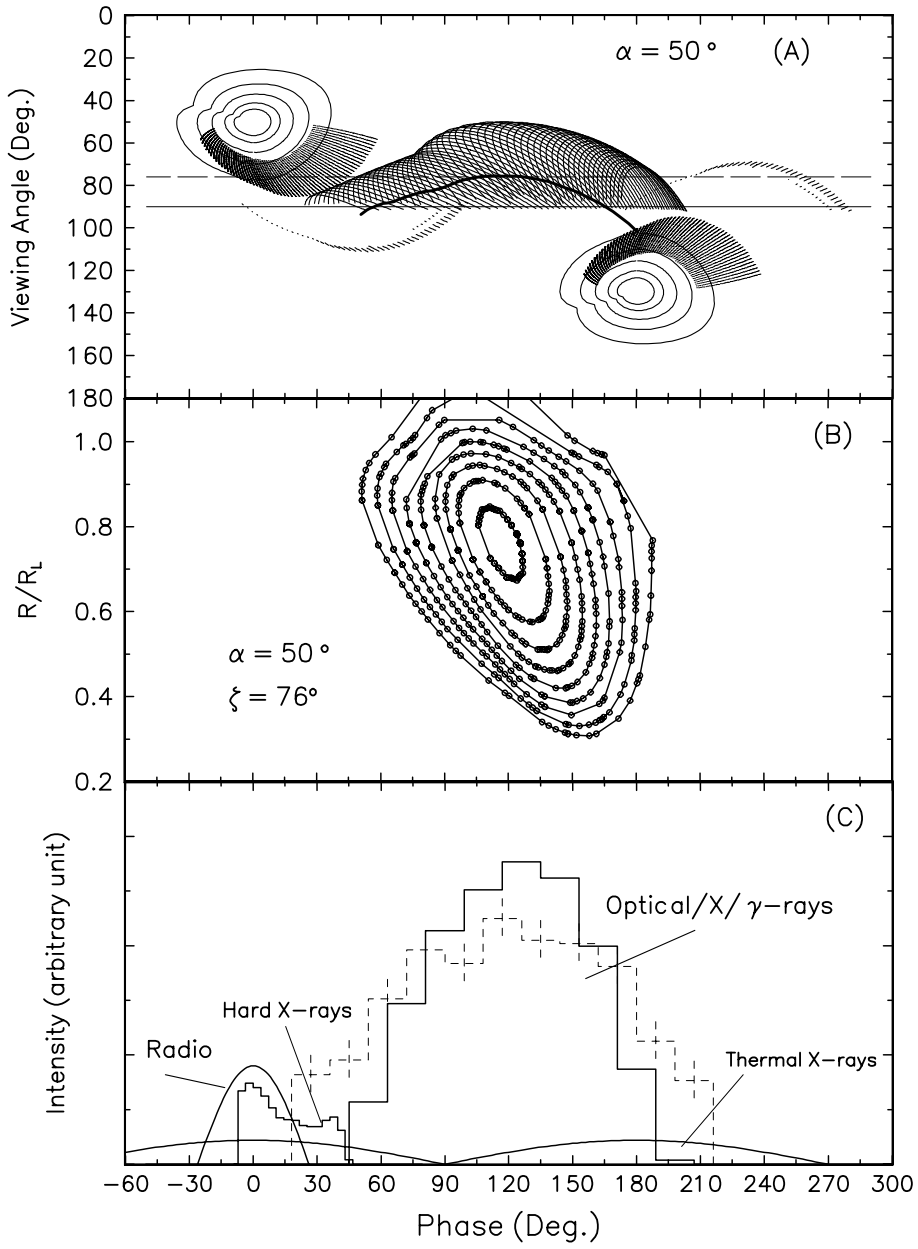

Fig. 6a–c. Emission projection onto the (ζ,Φ) plane and pulse profile for PSR B0540-69 ($\alpha = 50^\circ$). Panel A: Photon emission from the pulsar as a function of phase. The solid and dashed curves indicate inward and outward photon emission from the finite region above a single outer gap respectively. The tiny-solid curves represents inward and outward non-thermal photon emission from the region near the stellar surface. The observed lines of sight at $\zeta = 76^\circ$ and $\zeta = 90^\circ$ (dashed and solid lines), and both polar caps (contours) are shown. Panel B: The variation of radial distance with pulse phase for the thickness of the emission region of $\sim 0.21R_L$. The curves represent trajectories for $a_1 = 0.95$, 0.92, 0.89, 0.86, 0.83, 0.80, 0.77, 0.74 and 0.71 respectively. Panel C: Pulse profile for PSR B0540-69. The model optical/X-ray/γ-ray pulse at $\zeta = 76^\circ$ is shown. For comparison with the observed data, we have shown the observed pulse profile data for the X-ray band of 0.4 -10 KeV measured by Chandra (dashed histogram)(Gotthelf & Wang, 2000).

Here, we compare our results with those observed by Gotthelf & Wang (2000). To do this, we shift the observed pulse profile with respect to our expected results, then take 250 counts/sec as value of the X-ray background (see Fig. 4 of Gotthelf & Wang 2000). We then normalize the observed pulse profile so that its area is roughly same as that of the expected result at a phase of $\sim 45^\circ$ - $\sim 189^\circ$. The observed pulse profile is indicated by a dashed histogram with error bars in the panel C of Fig. 6.

We also model the phase-resolved and phase-averaged spectra of PSR B0540-69. First, we calculated the phase-resolved spectra for three phase bins: $\sim -15^\circ \leq \phi \leq \sim 50^\circ$, $\sim 60^\circ \leq \phi \leq \sim 180^\circ$, and $\sim 180^\circ \leq \phi \leq \sim 270^\circ$. In the phase bin from 180° to 270°, the photon emission is dominated by thermal photons coming from the stellar surface, the thermal spectrum is shown in Fig. 7. In the phase bin from $\sim -15^\circ$ to 50°, the photon emission is dominated by the non-thermal photon spectrum produced near the stellar surface due to the cascade process; the spectrum is shown in Fig. 8. One can see that the thermal component is negligible compared to the non-thermal component. In the phase bin from $\sim 60^\circ$ to $\sim 180^\circ$, the phase-resolved spectrum is dominated by the non-thermal photon emission above the outer gap (see Fig. 9). It can be seen that this photon emission is from optical to γ-ray range. In Fig. 9, the expected spectra for $\sin\beta(R_L) = 0.20$, 0.25 and 0.30 are shown.

Finally, we calculate the phase-averaged spectrum. The comparison with the observed data is shown in Fig. 10. Observed data at optical wavebands are taken from Middleditch et al. (1987), Hill et al. (1997). The data at the ROSAT energy range, the BeppoSAX energy range, and COMPTEL and EGRET are taken from Finley et al. (1993), Mineo et al. (1999),

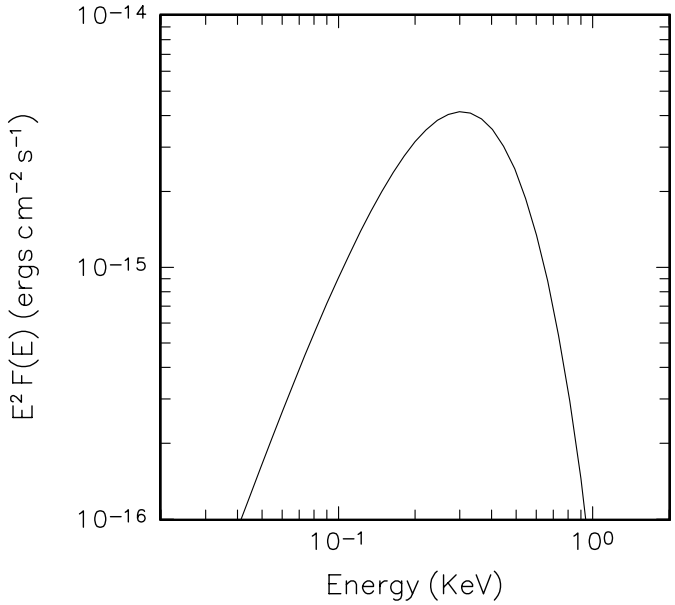

Fig. 7. Phase-resolved spectrum of PSR B0540-69 in the phase bin from $\sim 180^\circ$ to $\sim 270^\circ$. The photon emission in this phase bin is dominated by the thermal photons from the stellar surface.

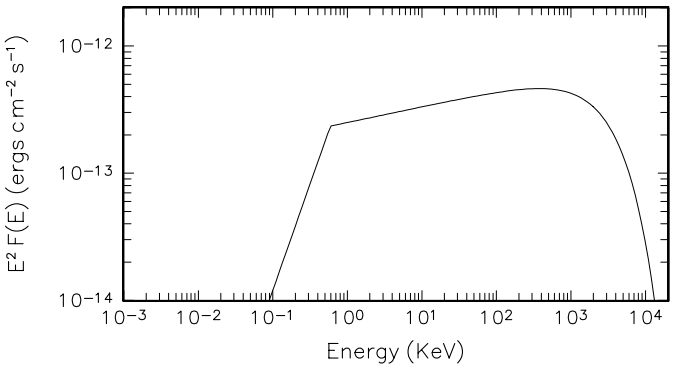

Fig. 8. Phase-resolved spectrum of PSR B0540-69 in the phase bin from $\sim -15^\circ$ to $\sim 50^\circ$. The photon emission in this phase bin is dominated by the non-thermal photons produced near the stellar surface. The beaming solid angle is assumed to be 1 sr.

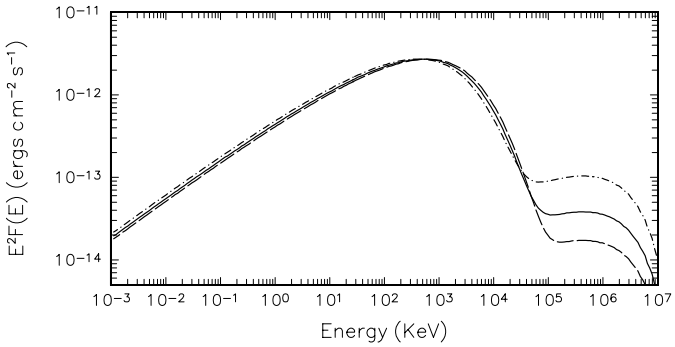

Fig. 9. Phase-resolved spectrum of PSR B0540-69 in the phase bin from $\sim 60^\circ$ to $\sim 180^\circ$. The photon emission in this phase bin is dominated by the non-thermal photons produced above the outer gap. The dot-dashed, solid, and dashed curves represent model results for $\sin(\beta(R_L)) = 0.20$, 0.25 and 0.30 respectively. The beaming solid angle is assumed to be 1 sr.

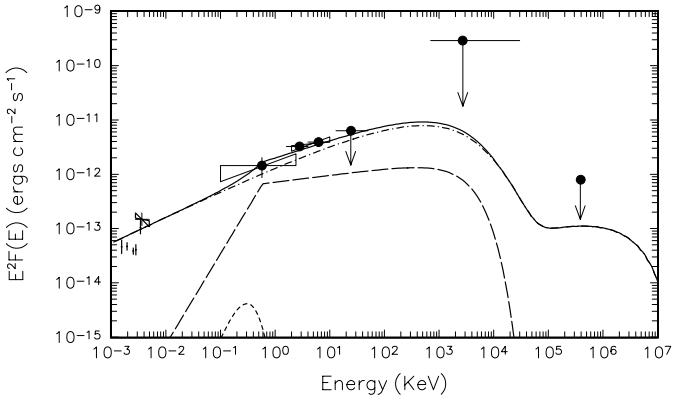

Fig. 10. The comparison of predicted phase-averaged spectrum with the observed data for PSR B0540-69. Observed data at optical waveband are taken from Middleditch et al. (1987), Hill et al. (1997). The data at ROSAT energy range, BeppoSAX energy range, COMPTEL and EGRET are taken from Finley et al. (1993), Mineo et al. (1999), Hermsen et al. (1994) and Thompson et al. (1994) respectively. The solid curve represents phase-averaged spectrum for $\sin(\beta(R_L)) = 0.25$. The dot-dashed, long-dashed and short-dashed curves represent photon spectra in different phases.

Hermsen et al. (1994) and Thompson et al. (1994) respectively. In Fig. 10, we show the three components. The fitting of the expected phase-averaged spectrum with the observed one gives a beaming solid angle of ~ 0.35 sr.

4. Summary

We have used a three-dimensional outer gap model to calculate the observed light curves and spectra of the Crab-like pulsars: PSR B1509-58 and PSR B0540-69. According to our model, there are three components for X-ray emission for Crab-like pulsars: thermal X-rays from the stellar surface, non-thermal X-rays produced near the stellar surface through synchrotron radiation and non-thermal photons produced above the outer gap through a synchrotron self-Compton mechanism. We have calculated the light curves and spectra of these three components for PSR B1509-58 and PSR B0540-69 respectively. Compared to non-thermal components, the thermal component can be negligible. Furthermore, the non-thermal photon emission above the outer gap dominates the non-thermal photons produced near the stellar surface. The light curves and spectra depend on the inclination angle (α), viewing angle (ξ) as well as the thickness of the emission region. We found that the inclination and viewing angles are 60° and 75° respectively and the mean thickness of the photon emission region is $\sim 0.11R_L$ for PSR B1509-58, and 50° and 76° respectively and $\sim 0.21R_L$ for PSR B0540-68. However, we stress that the observed light curves of these two pulsars are broader than our model light curves. If the radio beam is actually wider than $6.3^\circ/\sqrt{P}$ or radio emission comes from the region very near the stellar surface where multiple field dominates the dipolar field, a smaller inclination angle is

allowed and this gives a wider X-ray light curves (cf. Fig. 6 of CRZ).

Using the CHR model, Cheng & Ding (1994) and Cheng & Wei (1995) have calculated the phase-averaged spectrum of PSR B1509-58 by assuming that it is a Vela-like and a Crab-like pulsar respectively. Generally, if the mean distance to the outer gap approaches the light cylinder radius, and then the smaller magnetic field makes the Vela-like mechanism more favorable, otherwise the Crab-like mechanism is more likely. In their calculations, however, they did not consider the offset of the X-rays/γ-rays with respect to the radio pulse. Romani & Yadigaroglu (1995) have considered the observed offset and concluded that $\alpha = 60^\circ$ and $\xi \sim 75^\circ$ based on the geometry of the outer gap, which is consistent with our result. For PSR B0540-69, Cheng & Wei (1995) have calculated the phase-averaged spectrum by assuming that it is a Crab-like pulsar, which is consistent with our findings.

Acknowledgements. We thank R.W. Romani, M.A. Ruderman for useful discussion and suggestions, D.J. Thompson for providing the observed data of the multi-wavelength energy spectrum of PSR B1509-58. We thank the anonymous referee for his/her helpful comments. This work is partially supported by a RGC grant of the Hong Kong Government, a Croucher Foundation Senior Researcher Award, an Outstanding Researcher Award of the University of Hong Kong, Natural Science Foundation of Yunnan Province and National 973 project of China.

References

Becker W., Trümper J., 1997, A&A 326, 682
Carraminana A., Bennett K., Buccheri R., et al., 1995, A&A 304, 258
Carraminana A., Bennett K., Hermsen W., et al., 1997, In: Dermer C.D., Strickman M.S., Kurfess J.D. (eds.) AIP Conf. Proc. 410, Proceedings of the Fourth Compton Symposium, AIP, New York, p. 583
Cheng A.F., Ruderman M.A., Sutherland P.G., 1976, ApJ 203, 209
Cheng K.S., Ho C., Ruderman M.A., 1986a, ApJ 300, 500 (CHR I)
Cheng K.S., Ho C., Ruderman M.A., 1986b, ApJ 300, 522 (CHR II)
Cheng K.S., Ding W.K.Y., 1994, ApJ 431, 724
Cheng K.S., Wei D.M., 1995, ApJ 448, 218
Cheng K.S., Gil J., Zhang L., 1998, ApJ 493, L35
Cheng K.S., Zhang L., 1999, ApJ 515, 337
Cheng K.S., Ruderman M., Zhang L., 2000, ApJ 537, 964 (CRZ)
Chiang J., Romani R.W., 1992, ApJ 400, 724
Chiang J., Romani R.W., 1994, ApJ 436, 754
Deeter J.E., Nagase F., Boynton P.E., 1999, ApJ 512, 300
Eikenberry S.S., Fazio G.G., Ransom S.M., 1998, ApJ 492, 754
Finley J.P., Ögelman H., Hasinger G., Trümper J., 1993, ApJ 410, 323
Gotthelf E.V., Wang Q.D., 2000, ApJ 532, L117
Halpern J.P., Ruderman, M., 1993, ApJ 415, 286
Hermsen W., Kuiper L., Diehl R., et al., 1994, ApJS 92, 559
Hill R.J., Dolan J.F., Bless P.T., et al., 1997, ApJ 486, L99
Ho C., 1986, MNRAS 342, 396
Ho C., 1989, ApJ 221, 523
Holloway N.J., 1973, Nature Physical Science 246, 6
Kawai N., Okayasu R., Sekimoto Y., 1993, In: Friedlander M., Gehrels N., Macomb D.J. (eds.) AIP Conf. Proc. 280, Compton Gamma-Ray Observatory, AIP, New York, p. 204
Kuiper L., Hermsen W., Krijger J.M., et al., 1999, A&A 351, 119
Manchester R.N., Tuohy I.R., D'Amico N., 1982, ApJ 262, L31
Manchester R.N., Mar D.P., Lyne A.G., et al., 1993, ApJ 403, L29
Matz S.M., Ulmer M.P., Grabelsky D.A., et al., 1994, ApJ 434, 288
Middleditch J., Pennypacker C.R., 1985, Nat 313, 659
Middleditch J., Pennypacker C.R., Burns M.S., 1987, ApJ 315, 142
Mineo T., Cusumano G., Massaro E., et al., 1999, A&A 348, 519
Nagase F., Deeter J., Lewis W., et al., 1990, ApJ 351, L13
Nel H.I., Arzoumanian Z. Bailes M., et al., 1996, ApJ 898
Romani R.W., 1996, ApJ 470, 469
Romani R.W., Yadigaroglu I.-A., 1995, ApJ 438, 314
Rots A.H., Jahoda K., Macomb D.J., et al., 1998, ApJ 501, 749
Saito Y., 1998, Ph.D Thesis
Seward F.D., Harnden F.R., 1982, ApJ 256, L45
Seward F.D., Harnden F.R., Helfand D.J., 1984, ApJ 287, L19
Thompson D.J., Arzoumanian Z., Bertsch D.L., et al., 1994, ApJ 436, 229
Thompson D.J., Bailes M., Bertsch D.L., et al., 1999, ApJ 516, 297
Ulmer M.P., Matz S.M., Wilson R.B., et al., 1993, ApJ 417, 738
Wang F.Y.-H., Ruderman M., Halpern J.P., Zhu T., 1998, ApJ 498, 373
Zhang L., Cheng K.S., 1997, ApJ 487, 370 (ZC)
Zhang L., Cheng K.S., 1998, MNRAS 294, 177